Optical interferometry–based array of seafloor environmental sensors using a transoceanic submarine cable

Title: Optical interferometry-based array of seafloor environmental sensors using a trans-oceanic submarine cable

Authors: G. Marra[1*], D. M. Fairweather[2], V. Kamalov[3], P. Gaynor[1], M. Cantono[3], S. Mulholland[1], B. Baptie[4], J. C. Castellanos[3], G. Vagenas[1], J-O. Gaudron[1], J. Kronjäger[1], I. R. Hill[1], M. Schioppo[1], I. Barbeito Edreira[1], K. A. Burrows[1], C. Clivati[5], D. Calonico[5], A. Curtis[2]

Affiliations:
[1]National Physical Laboratory; Teddington, UK

[2]University of Edinburgh, School of GeoSciences; Edinburgh, UK

[3]Google LLC; Mountain View, CA, USA

[4]British Geological Survey; Edinburgh, UK

[5]Istituto Nazionale di Ricerca Metrologica; Turin, Italy

*Corresponding author. Email: giuseppe.marra@npl.co.uk

Abstract: Optical fiber-based sensing technology can dramatically improve Earth observations by enabling the use of existing submarine communication cables as seafloor sensors. Previous interferometric and polarization-based techniques demonstrated environmental sensing over cable lengths up to 10,500 km. However, measurements were limited to the integrated changes over the entire length of the cable. We demonstrate the detection of earthquakes and ocean signals on individual spans between repeaters of a 5,860 km-long transatlantic cable, rather than the whole cable. By applying this technique to the existing undersea communication cables, which have a repeater-to-repeater span length of 45 to 90 km, the largely unmonitored ocean floor could be instrumented with thousands of permanent real-time environmental sensors without changes to the underwater infrastructure.

One-Sentence Summary: Detection of earthquakes, microseisms and water currents on individual spans of a 5,860 km-long subsea optical fiber link.

Main Text:

Despite substantial expansion of sensing capabilities, seas and oceans remain mostly unmonitored, limiting our understanding of the Earth's structure and its dynamic behavior. However, research on techniques exploiting the sensitivity of optical fiber to environmental perturbations over the past few years has shown that the existing network of submarine cables could potentially be used as seafloor sensors. While backscattering-based techniques, such as Distributed Acoustic Sensing (DAS), provide high sensitivity and spatial resolution, such approaches are currently limited to coastal areas up to 100 km from the shore due to signal attenuation (*1-4*). Previously, we showed that optical interferometric techniques, which detect optical phase changes, provide a solution for monitoring over much longer distances than the working range of DAS, but at the expense of a lower spatial resolution (*5*). More recently, Zhan et al. demonstrated that polarization of light can also be used for environmental sensing over submarine cables up to 10,500 km long (*6*). However, in both techniques, the measured quantity is the cumulative phase or polarization change over the entire length of the optical fiber cable. Whilst the detection of earthquakes and ocean waves were successfully demonstrated, measuring the integrated perturbations over the entire cable length has two major limitations. First, the measurement noise floor is set by the background environmental noise integrated over the entire cable length. This limits the detection of smaller-sized earthquakes and other environmental signals of interest. Second, because the cable acts as a single sensor, signals from multiple cables are required to triangulate the location of sources, such as earthquake epicenters (*5*).

Our work overcomes the first limitation and substantially improves on the second, by using an optical technique that enables the measurement of environmentally-induced optical phase changes over individual sections of the submarine cable rather than its entire length. In doing so, we demonstrate the detection of earthquakes, microseisms, and ocean currents spatially resolved at several locations along the cable. We show that the substantially higher sensitivity achieved by this interferometry-based technique enables the detection of signals that could not be observed when measuring the cumulative optical perturbation across the entire cable. Lastly, we show that, by performing span-wise measurements, a single cable is sufficient to identify the epicentral region of a teleseismic earthquake.

The cable sections correspond to one or more spans between the repeaters used for the amplification of the optical signal along the cable. The technique we used allows for the environmentally-induced optical perturbations in each cable section to be measured independently, effectively converting a submarine cable into an array of fiber-based sensors. The number of sensors can be as high as the number of repeater-to-repeater cable spans. For an intercontinental link, such as the one we used, the number of spans can exceed 100. The technique we present has the potential to transform our Earth monitoring capabilities, as the currently greatly under-sampled seafloor could be instrumented with thousands of interferometry-based sensors without modifying the existing submarine telecommunication infrastructure. Crucially, whilst in our work we used a research-grade ultrastable laser, we show that more compact and lower cost narrow-linewidth telecommunications lasers could also be used with limited or no loss of sensitivity. This feature makes our technique highly scalable towards potential conversion of the existing subsea cable infrastructure into a global network of environmental sensors.

We achieve an array of sensing elements by exploiting the architecture of repeaters in modern submarine cables. These often include a high-loss loop back path (HLLB) which enables a small fraction of the transmitted light to be returned to the transmitting end via the second fiber of the fiber pair (Fig. 1). On many cables the return path is implemented by employing fiber Bragg gratings (FBG), acting as narrow band reflectors (fig. S1A). These return paths are used by the cable operator to periodically check the health of the optical amplifiers (*7*). These checks are typically performed on a schedule or if there is a malfunction, leaving these channels unused most of the time. By injecting infrared light from an ultrastable laser source and performing high-precision interferometric measurements of the signal returned by the HLLBs, we extract the round-trip (loop-back) accumulated optical phase changes in the fiber between the transmitter end of the cable and the chosen repeaters. In order to localize the perturbations to cable sections between two or multiple repeaters, we compute the difference between loop-back signals. As the wavelength of the FBG reflectors is the same for all HLLBs, we employ an optical technique, known as Optical Frequency Domain Reflectometry (*8*), whereby the frequency of the light source is swept such that the loop-back signal from each repeater can be separated in the frequency domain. This technique is used in some Rayleigh scattering-based fiber sensing applications (*9*). However, in our test we do not use the scattered light from the fiber inhomogeneities, but the signal returned by the FBG-based reflector in the HLLBs. This results in a returned signal that is orders of magnitude higher in amplitude than from back-scattering. The frequency-swept laser light is injected into the forward path of the submarine cable. The light returned at the transmitter, which consists of the overlap of the returned light from each repeater, is combined on a photodetector with the output of the swept laser. Here, a series of radio frequency signals is obtained where each frequency identifies a different repeater with

frequency proportional to the round-trip time (fig. S2). Each loop-back beat note is spectrally filtered and its phase, relative to that of the local laser source, is measured with a phase meter.

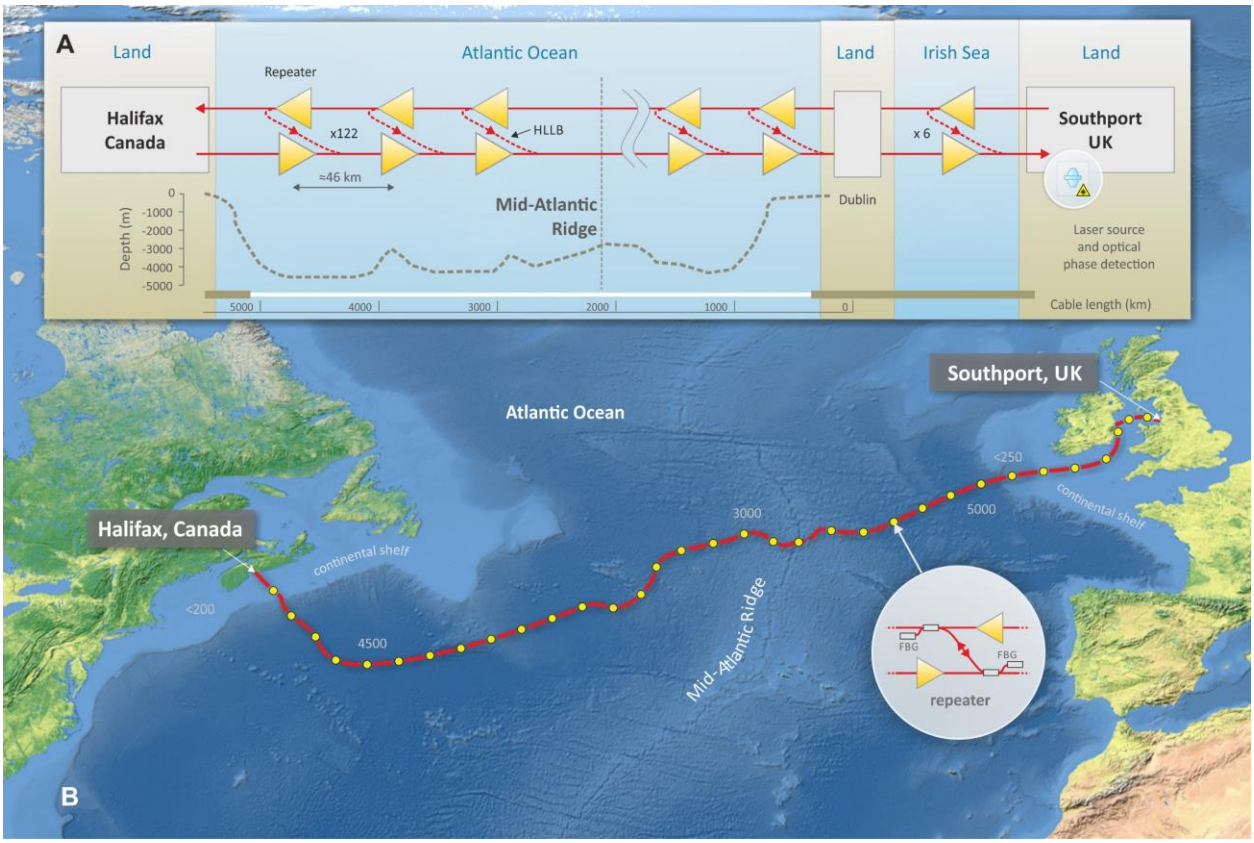

Fig. 1. Map and details of the UK-Canada submarine link. (**A**) Illustration of the high-loss loop-back (HLLB) architecture and cable bathymetry. (**B**) Map of the UK-Canada submarine cable. The actual number of repeaters (128) was reduced in the figure for illustration purposes. Each repeater has a pair of fiber Bragg grating reflectors (FBG).

We tested this technique on a 5,860 km-long intercontinental submarine optical fiber link between the UK and Canada. The link consists of two cables: a 248 km-long cable from Southport, UK, to Dublin, Ireland, and a 5,611 km-long cable from Dublin to Halifax, Canada. A total of 128 optical repeaters are installed on the link and the average span between them is 46 km. Our current experimental setup allows us to simultaneously measure loop-back signals from up to 12 repeaters

at a time, which can be selected. The hardware upgrades required to extend the monitoring capability to the full number of spans between repeaters are shown in fig. S3. Because of temperature-induced polarization changes in the cable, the signal-to-noise ratio (SNR) of some of the available loop-back signals can temporarily become insufficient for the frequency counter to perform a correct measurement. In our tests, on average, 7 to 9 loop-back signals exhibit sufficient SNR. Moreover, the SNR of the returned signal degrades due to the accumulation of amplified spontaneous emission (ASE) noise of the optical amplifiers for repeaters increasingly distant from the transmitting end. In our tests we obtain signals with sufficient SNR from repeaters at a cable distance up to 3,100 km. As this is more than half of the cable length, monitoring of all the submarine cable spans could be achieved by measuring also from the Canadian end. Both the polarization-induced degradation of the signal and the range of usable loop-back signals can be, respectively, eliminated and extended with further upgrades (*10*). We also successfully tested our technique while data traffic was present on other channels available in the fiber pair. This demonstrates the compatibility of our technique with standard optical communication technology, which is a crucial prerequisite for its wide application over the submarine telecommunication network.

We show the detection of two earthquakes on multiple submarine cable spans, the Northern Peru Mw 7.5 earthquake (28th November 2021) and the Flores Sea Mw 7.3 (14th December 2021), respectively (Figs. 2A, B). We detected the Northern Peru earthquake on 6 of the 9 sections of the cable under test. We plotted a spectrogram and time series of the signals detected by 3 of these sections (Fig. 2A). The signals and location of the additional 6 spans are shown in fig. S4. The spectrograms display the temporal evolution of the power spectral density (PSD) of the frequency fluctuations of the optical signal, induced by environmental perturbations, over the cable section that is being measured. For all the data shown in this work, we choose to display the optical

frequency deviation rather than phase deviation, as we experimentally find that this allows us to better visualize significant features in the detected signals. Several factors can contribute to the amplitude of the observed waveform, including the earthquake fault geometry, the 3-dimensional heterogeneity of the seismic structure between the fault and cable, the coupling of cable to the external environment, and the length of the fiber. Further tests on a larger number of spans and events will allow better characterization of the weight of each contribution. From the time lag between envelopes of the detected teleseismic P-waves (Fig. 2A) and via a simple back-projection (BP) approach (10), we are able to resolve the epicentral location of the seismic event (Fig 2D).

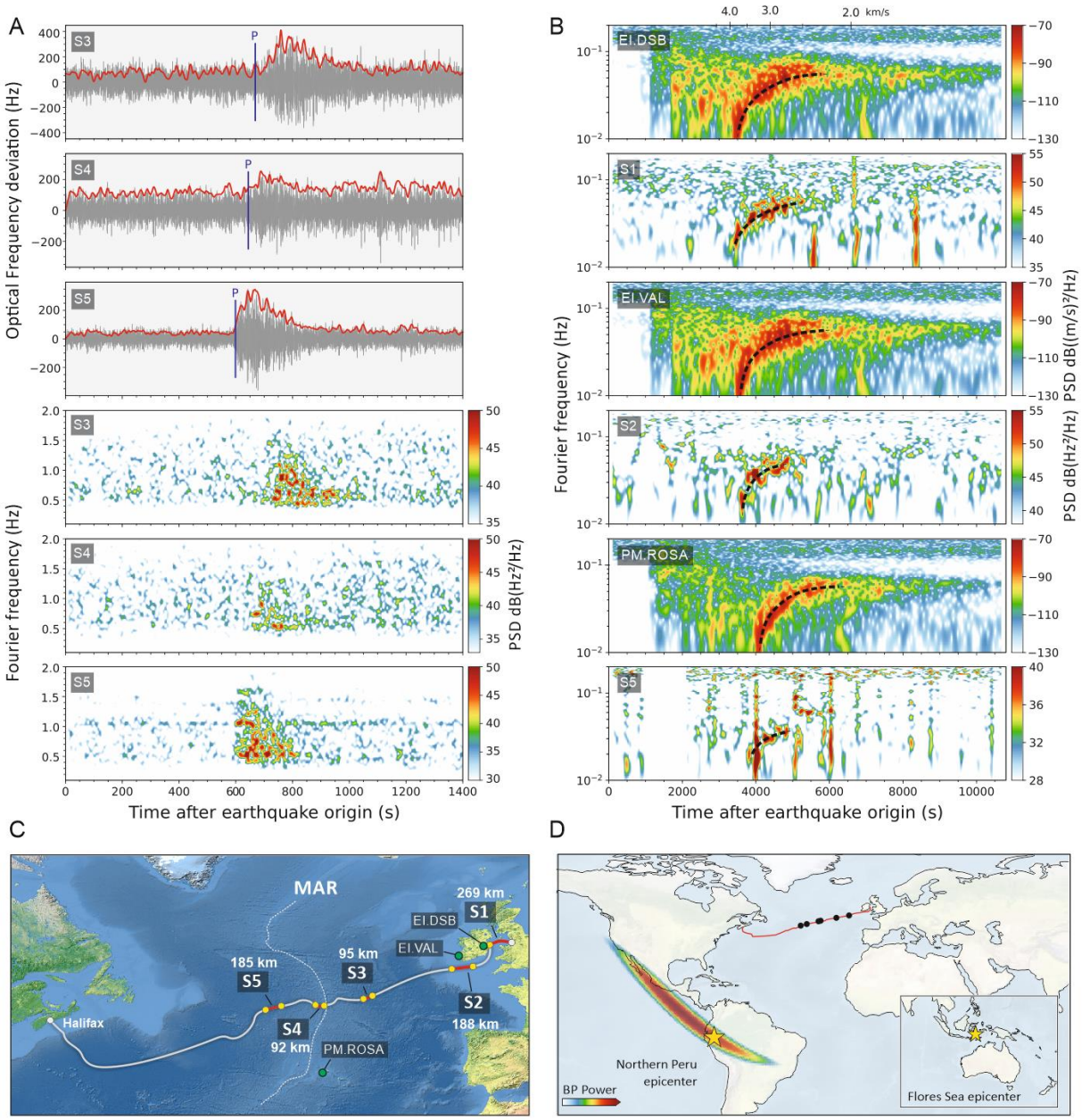

Fig 2. Earthquake detections on submarine cable spans. (**A**) Time series and spectrograms of the optical frequency deviation induced by the Northern Peru earthquake detection. Vertical blue lines show the theoretical P-wave arrival time. (**B**) Spectrograms of the Flores Sea earthquake detected by the cable sections and compared to their nearest seismic stations on land. The dashed black lines on the spectrograms track the surface wave group velocity dispersion. As a reference, we show the group velocity scale for station EI.DSB. (**C**) Map of the cable sections used for data

displayed in A and B and location of the seismometers considered in B. (**D**) Geographical area for the epicenter location for the Northern Peru earthquake, obtained by back-projection. The heatmap represents the probability of the epicenter location, with hot colors representing a higher probability. The stars indicate the event epicenters as reported by the GCMT earthquake catalog (*11*,*12*), and the black dots show the locations of the 6 cable sections used for the BP (*10*).

The Flores Sea earthquake was detected on 5 of the 9 cable sections under test (fig. S7). The spectrogram of the optical frequency deviations (Fig. 2B) induced by the seismic wave on the S1, S2 and S5 cable sections (Fig. 2C) is shown in comparison with the closest available seismic station on land. Whilst the P-wave arrival is not visible on the span data, the surface wave dispersion is clearly resolved and shows very good agreement with that measured by land seismometers. In addition to the measurements on separate sections of the cable, we also measure the optical frequency changes on the entire UK-Canada cable on a separate channel of the same fiber pair. We perform this measurement by connecting the fiber pair together at the Halifax end, such that we obtain a return signal in Southport after a 11,720 km-long round trip. We stress that in this arrangement the signal does not go through the HLLBs but forward propagates for the entire length of the cable, as in our previous work (*5*). Whilst the surface wave of the Flores Sea earthquake was also visible on the entire cable measurement (fig. S7), the Northern Peru earthquake was not detected (fig. S4). This is because the detected surface waves from the Flores Sea signal have components between 0.01 and 0.1 Hz, which we measure to be a relatively low noise frequency range on the seafloor, whilst the detected body waves from the Northern Peru signal have components in the 0.1-5 Hz range, which is significantly noisier. The detection of the Northern Peru earthquake therefore demonstrates the substantially better

detection threshold achieved with span-wise measurements, as the background environmental noise on the other parts of the cable does not contribute to the measurement noise floor.

We show the spectrogram of the environmental noise measured by different sections of the intercontinental submarine cable from the cable landing station (CLS) in Southport to the Mid-Atlantic Ridge (MAR) on 21st October 2021 (Fig. 3). On the first 269 km cable section, which crosses the Irish Sea floor, we observe narrow-band components in the 1-5 Hz range which repeat approximately every 6 hours (Fig. 3A). This periodic pattern is synchronous with tidal currents in the Irish Sea and their amplitude correlates well with the neap/spring cycle, as shown by a longer data set in Fig. 4A. We speculate that the observed signals arise from “strumming” of exposed cable sections or pressure changes induced by the tidal currents. We observe these periodic signals also on the second section close to the southeastern coast of Ireland (Fig. 3B) although less pronounced, and a strong microseismic component in the 0.07-0.15 Hz range. This last feature is likely to be caused by the coupling of ocean wave energy to the shallow seafloor.

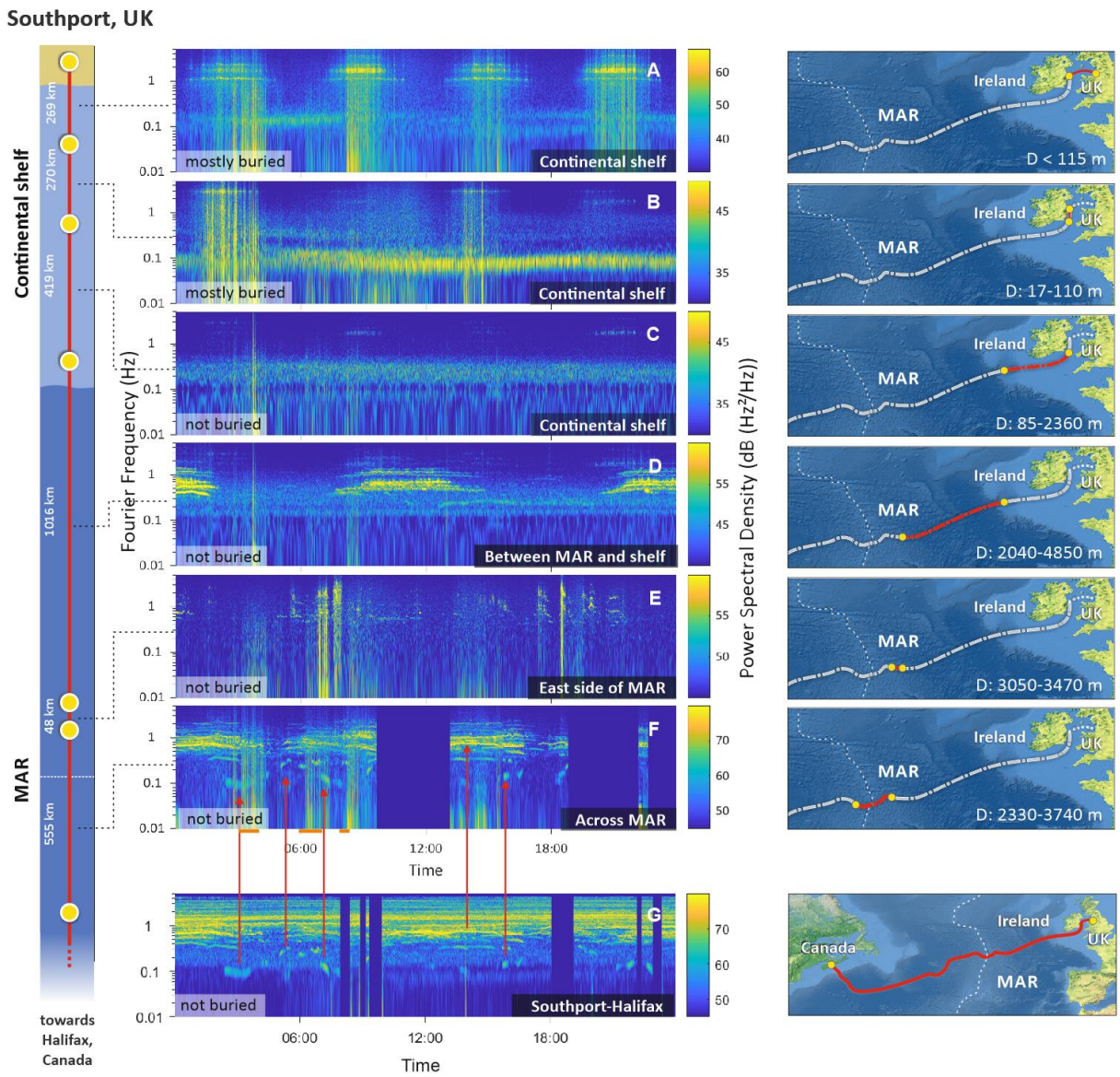

Fig. 3. Environmental noise detected by different sections of the trans-Atlantic cable. Environmental noise detected on continental shelf, deep ocean and mid-Atlantic ridge sections of the cable. Data with insufficient SNR was removed. The range of the color bar of each spectrogram is adjusted to best visualize the detected signals. The impulsive noise in the spectrograms corresponding to the time marked by the short horizontal orange lines at the bottom of panel F is due to glitches caused by temporary issue with the laser locking setup and not to environmental noise on the seafloor.

On the cable section that extends from off the Irish coast to the end of the continental shelf, where the bathymetry is consistently flat, we observe a drop in the environmental noise level of up to 30 dB (Fig. 3C and fig. S8). On the fourth section (Fig. 3D), extending from the end of the continental shelf to the MAR area, we detect excess noise between 0.5 and 1.5 Hz, this time with a 12 h repeating pattern, which we attribute to tidal currents in the MAR area. We also observe a significant increase in the detected noise as the cable approaches and crosses the MAR (Fig. 3E, F). We attribute this to the interaction of ocean currents with the changing MAR bathymetry. Around this area, sea mounts rise from 3740 to 2330 m water depth, with the cable possibly being suspended between irregularities of the seafloor and thus more subject to current-induced movement. By comparison of Fig. 3F and Fig. 3G, we can identify several features on the spectrogram of the integrated round-trip signal over the entire Halifax-Southport cable (Fig. 3G) on that of the cable section across the MAR (Fig. 3F), indicating that this area is a large contribution to the overall measured noise. We also observed a high level of correlation of the periodic signals observed on the shallow water sections of the cable with the tidal current velocity (Fig. 4A). We also found a high level of correlation between the signals in the 0.1-0.5 Hz range and the wave height measured at the M2 buoy in the Irish Sea (Fig. 4A). We identified Hurricane Larry to be the likely source of the dispersive microseism in the 0.05-0.1 Hz frequency range between 13th and 17th September (*10*). We show an 8 day-long data set in late November 2021 (Fig. 4B), on the cable section shown in Fig. 4D. During this time an extratropical cyclone moved southwards across the UK and a resulting strong microseism component was observed on the Southport-Dublin section of the cable. This correlates very well with the increase of average wave height measured at the M2 buoy.

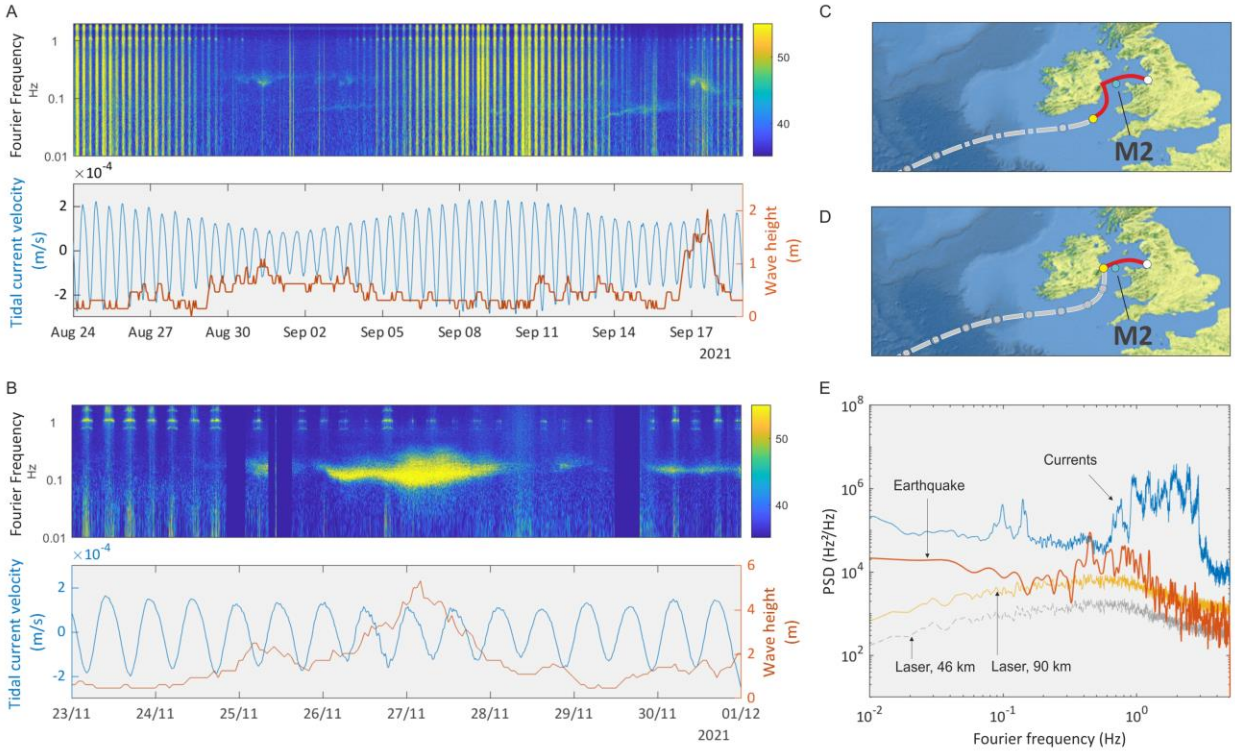

Fig 4. Correlation of detected signals on cable spans with wave height and tidal currents. (**A**) Spectrogram of the frequency changes detected on the span shown in C compared to wave height measured at the M2 buoy in the Irish Sea and tidal current velocity measured by the Dublin Port tide gauge, showing a high degree of correlation. (**B**) Storm detected on the span shown in D in late November 2021 and correlation with water levels and tidal current velocity measured in the Irish Sea. (**C**, **D**) Maps of the cable sections used and M2 buoy. (**E**) Comparison between the power spectral density of environmental signals (earthquake and currents) and the calculated measurement noise floor that would be obtained if an off-the-shelf telecommunication narrow-linewidth laser, instead of research-grade laser, were used on a 46 km and 90 km span (*10*).

Crucially, in contrast to previous optical interferometric tests, which required a research-grade ultrastable laser (*5*), the technique we have demonstrated greatly relaxes the requirements on the laser source. Because the optical perturbations are measured over sections of the cable rather than the whole length, the requirement for the laser coherence length is scaled accordingly (*10*). For the submarine cable used in these tests, the coherence length requirement is reduced by approximately a factor of 129, equating to the number of ~46 km-long spans between repeaters and to the CLSs. While in our experiment we still used a research-grade stabilized laser developed at NPL, we show that commercially available narrow-linewidth lasers could be used instead to detect most of the signals we have presented. An example is in the PSD of the Mw 7.5 Peru earthquake (Fig. 4E) detected on the 95 km-long S3 span of Fig. 2C. For comparison, the contribution of the laser instability of a narrow-linewidth telecommunication laser to the measurement noise floor over the same span length is displayed. We also show the PSD of the current-induced noise measured over the 92 km-long S4 span west of MAR, which are up to 30 dB above the expected laser contribution to the noise floor.

By enabling the use of commercially available telecommunication lasers, our technique could easily be scaled up and applied to a large number of cables in the existing submarine network. By converting submarine cables into arrays of environmental sensors, a large network of hundreds or thousands of permanent and real-time seafloor sensors could be implemented without modification of the existing subsea infrastructure. This has the potential to transform our understanding of both shallow and deep processes inside the Earth. The ability to record seismic phases in the middle of ocean basins could enable the imaging of previously obscured structures such as mid-ocean ridges and oceanic fault zones, advancing our understanding of the processes that underlie the generation of oceanic crust (*13*), and the mechanisms by which oceanic plates are hydrated (*14*).

The cable sensitivity to water currents could be explored to improve our understanding of deep-water flows (thermohaline circulation), including the proposed slowing down of ocean currents due to rising global temperatures (*15,16*). Furthermore, the joint detection of deep-water currents and seafloor pressure changes caused by the passing of ocean waves implies strong potential for tsunami sensing (*17,18*). Lastly, whilst more research is needed to characterize long-term measurement drifts (10), the sensitivity of the optical cables to temperature could be explored for climate change research (18,20).

References and Notes

1. E. F. Williams *et al.*, Distributed sensing of microseisms and teleseisms with submarine dark fibers, *Nature communications*, **10**, 1-11 (2019), doi: https://doi.org/10.1038/s41467-019-13262-7

2. N. J. Lindsey, T. C. Dawe, and J. B. Ajo-Franklin, Illuminating seafloor faults and ocean dynamics with dark fiber distributed acoustic sensing, *Science* **366,** 1103-1107 (2019), doi: 10.1126/science.aay5881

3. 1. Z. J. Spica, K. Nishida, T. Akuhara, F. Pétrélis, M. Shinohara, T. Yamada. Marine Sediment Characterized by Ocean-Bottom Fiber-Optic Seismology, *Geophysical Research Letters*, **47** (2020), doi: doi.org/10.1029/2020GL088360.

4. E. F. Williams *et al.*, Scholte wave inversion and passive source imaging with ocean-bottom DAS, *The Leading Edge*, **40**(8), 576-583 (2021), doi: doi.org/10.1190/tle40080576.1

5. G. Marra *et al.*, Ultrastable laser interferometry for earthquake detection with terrestrial and submarine cables, *Science*, **361** (2018), doi: 10.1126/science.aat4458

6. Z. Zhan et al., Optical polarization-based seismic and water wave sensing on transoceanic cables, *Science*, **371** 931-936 (2021), doi: 10.1126/science.abe6648

7. José Chesnoy, *Undersea Fiber Communication Systems* (Academic Press, 2016), pp. 651-669

8. W. Eickhoff and R. Ulrich, Optical frequency domain reflectometry in single-mode fiber, *Applied Physics Letters* **39**, 693-695 (1981), doi: doi.org/10.1063/1.92872

9. Z. Ding *et al.*, Distributed Optical Fiber Sensors Based on Optical Frequency Domain Reflectometry: A review, *Sensors* **18**(4), 1072 (2018), doi: doi.org/10.3390/s18041072

10. Materials and methods are available as supplementary materials at the Science website

11. A.M. Dziewonski, T.-A. Chou, J. H. Woodhouse, Determination of earthquake source parameters from waveform data for studies of global and regional seismicity, *Journal of Geophysical Research*, **86**, 2825-2852 (1981), doi: doi.org/10.1029/JB086iB04p02825

12. G. Ekström, M. Nettles, A. M. Dziewonski, The global CMT project 2004-2010: Centroid-moment tensors for 13,017 earthquakes, *Physics of the Earth and Planetary Interiors*, **200-201**, 1-9, (2012), doi: doi.org/10.1016/j.pepi.2012.04.002

13. Searle, R. C., and A. V. Bralee, Asymmetric generation of oceanic crust at the ultra-slow spreading Southwest Indian Ridge, 64° E., *Geochemistry, Geophysics, Geosystems* **8,** (2007), doi: dx.doi.org/10.1029/2006GC001529

14. Eakin, Caroline M., Catherine A. Rychert, and Nicholas Harmon, The role of oceanic transform faults in seafloor spreading: A global perspective from seismic anisotropy, *Journal of Geophysical Research: Solid Earth* **123**, 1736-1751 (2018), doi: doi.org/10.1002/2017JB015176

15. J.R. Toggweiler, R.M. Key, "Thermohaline Circulation", *Encyclopedia of Ocean Sciences*, (Academic Press, 2001), pp 2941-2947, doi: doi.org/10.5670/oceanog.2002.08

16. J.M. Gregory, R. Tailleux, Kinetic energy analysis of the response of the Atlantic meridional overturning circulation to CO2-forced climate change, *Climate Dynamics* **37**, 893–914 (2011). doi: 10.1007/s00382-010-0847-6

17. A. B. Rabinovich, M. C. Eblé, Deep ocean measurements of tsunami waves, *Pure and Applied Geophysics*. **172**, 3281–3312 (2015), doi: 10.1007/s00024-015-1058-1

18. R. E. Thomson *et al.*, Observations of the 2009 Samoa tsunami by the NEPTUNE-Canada cabled observatory: test data for an operational regional tsunami forecast model, *Geophysical Research Letters* **38**, L11701 (2011)**,** doi: doi.org/10.1029/2011GL046728

19. Wu, Wenbo, Zhongwen Zhan, Shirui Peng, Sidao Ni, and Jörn Callies, Seismic ocean thermometry, *Science* **369**, 1510-1515 (2020), doi: doi.org/10.1126/science.abb9519

20. C. S. Meinen, R. C. Perez, S. Dong, A. R. Piola, E. Campos, Observed ocean bottom temperature variability at four sites in the Northwestern Argentine basin: Evidence of decadal deep/abyssal warming amidst hourly to interannual variability during 2009–2019, *Geophysical Research Letters*, **47**, (2020), doi.org/10.1029/2020GL089093

21. Ishii, Miaki, Peter M. Shearer, Heidi Houston, and John E. Vidale, Extent, duration and speed of the 2004 Sumatra–Andaman earthquake imaged by the Hi-Net array, *Nature* **435**, no. 7044, 933-936 (2005), doi: dx.doi.org/10.1038/nature03675

22. Y. Han, J. C. Castellanos, C. Yu, L. Meng, Z. Zhan, Localized water reverberation phases and its impact on backprojection images, *Geophysical Research Letters* **44**, no. 19, 9573-9580 (2017), doi: doi.org/10.1002/2017GL073254

23. J. C. Castellanos, Z. Zhan, W. Wu, Absolute centroid location of submarine earthquakes from 3D waveform modeling of water reverberations, *Journal of Geophysical Research: Solid Earth* **125**, no. 5 (2020), doi: doi.org/10.1029/2019JB018941

24. L. M. Cathles IV, E. A. Okal, D. R. MacAyeal, Seismic observations of sea swell on the floating Ross Ice Shelf, Antarctica, *Journal Geophysical Research*, **114**, F02015 (2009), doi: dx.doi.org/10.1029/2007JF000934

25. H. Hersbach *et al.*, (2018): ERA5 hourly data on single levels from 1979 to present. Copernicus Climate Change Service (C3S) Climate Data Store (CDS), doi: doi.org/10.24381/cds.adbb2d47

26. B. Pérez, E. Álvarez Fanjul, S. Pérez, M. de Alfonso, J. Vela, Use of tide gauge data in operational oceanography and sea level hazard warning systems, *Journal of Operational Oceanography*, **6**, 1-18 (2013), doi: 10.1080/1755876X.2013.11020147

27. E. Bernard *et al*., Tsunami resilient communities, in OceanObs '09: Sustained Ocean Observations and Information for Society, 58–70 (2010). doi: doi.org/10.5270/OceanObs09.pp.04

28. F. Stefani *et al.*, Tackling the limits of optical fiber links, *Journal of the Optical Society of America B* **32**, 787-797 (2015), doi: doi.org/10.1364/JOSAB.32.000787

29. N. Lagakos, J. A. Bucaro, Pressure desensitization of optical fibers, *Applied Optics* ***20***, 2716-2720 (1981), doi: doi.org/10.1364/AO.20.002716

30. X. Cheng, N. Ou, J. Chen, R. X. Huang, On the seasonal variations of ocean bottom pressure in the world oceans, *Geoscience Letters* **8**, 29 (2021), doi.org/10.1186/s40562-021-00199-3

Acknowledgments: We thank J. Tunesi and R. M. Godun (NPL) for careful reading of the manuscript and S. Robinson for useful discussions. We thank the NPL IT team for help setting up the NPL-Southport remote access capabilities. We thank U. Hölzle, B. Koley, V. Vusirikala

(Google LLC) for support and discussions, D. Lloyd, M. Cox, T. Dickenson, M.Wildman, L. Taylor, A. Walsh (GTT) and T. Aydin (Google LLC) for support on setting up the experiments on the UK-Canada cable. **Funding:** NPL: This work was supported by an ISCF Metrology Fellowship grant and as part of the National Measurement System Programme provided by the UK government's Department for Business, Energy and Industrial Strategy (BEIS), and by an Award from the National Physical Laboratory's Directors' Science and Engineering Fund. University of Edinburgh: This work was supported by the Engineering and Physical Sciences Research Council Doctoral Training Project EP/T517884/1. British Geological Survey: this work is funded by the Natural Environment Research Council (NERC). INRIM: This project receives funding from the European Union's Horizon 2020 research and innovation programme under Grant Agreement No. 951886 (CLONETS-DS). **Author contributions:** G.M., V.K., M.C., D.C. planned and designed the work. G.M., S.M., P.G. designed the experimental setup. P.G., S.M., G.V., J-O.G., I.B.E., M.S., I.R.H., G.M. built the experimental setup. G.M., P.G., J-O.G., conducted the experiments. G.M., J.K., C.C., D.C. provided frequency metrology expertise, G.M., D.F., B.B., J.C.C. prepared the initial draft and all authors critically reviewed and approved the manuscript. D.F., A.C., B.B., J.C.C., G.M., V.K., M.C., K.A.B. analyzed the data. **Competing interests:** A UK priority patent application has been filed in relation to this work. **Data and materials availability:** All data are available at 10.5281/zenodo.6405431

List of Supplementary materials:

Materials and Methods

Supplementary Text

Fig. S1 to S13

References: 21-30

Science
AAAS

Supplementary Materials for

Optical interferometry-based array of seafloor environmental sensors using a trans-oceanic submarine cable

G. Marra*, D. M. Fairweather, V. Kamalov, P. Gaynor, M. Cantono, S. Mulholland, B. Baptie, J. C. Castellanos, G. Vagenas, J-O. Gaudron, J. Kronjäger, I. Hill, M. Schioppo, I. Barbeito Edreira, K. Burrows, C. Clivati, D. Calonico, A. Curtis

Correspondence to: giuseppe.marra@npl.co.uk

This PDF file includes:

Materials and Methods
Supplementary Text
Figs. S1 to S13

Materials and Methods

Operating principle and optical setup

The High-Loss Loop Back HLLB topology of the submarine cable used in our tests is shown in fig. S1A. The HLLB returns less than 1/100 of the power of the signal available at the output of the optical amplifier (Out 1) at the wavelength of 1561 nm set by the Fibre Bragg Grating (FBG). The attenuator is added to compensate for manufacturing tolerances in the coupling ratio of the optical coupler. The topology is symmetric for both directions of propagation, defined by the direction of the optical amplifiers.

A top-level illustration of the loop-back architecture is shown in Fig. S1B. In order to isolate the signal detected by each repeater-to-repeater span, we subtract the loop-back signals from two chosen repeaters. For example, the induced optical perturbations over Span 2 can be extracted by difference of the loop back signals from repeaters B and A.

The center wavelength of the fiber Bragg grating in the cable HLLB is the same for all repeaters. In order to separate the signals returned from each HLLB we scan the laser frequency in a saw-tooth fashion as shown in Fig S2A. We split the power of the frequency-swept source into two arms, one consisting of the submarine cable and a reference arm. By recombining these two signals, a series of radio frequency (RF) signals is generated, one for each return signal received from the HLLBs. The frequency of each tooth is proportional to the delay experienced by each loop-back signal, showing as f1 and f2 in Fig. S2A. We use an electro-optical modulator (EOM) to sweep the frequency rather than directly modulate the laser current. This is because the non-linearity of the current-to-frequency response of the laser leads to errors in the measured loop-back signal larger than the changes to be measured. By driving the EOM with a good quality RF generator these errors become negligible.

By employing the swept-frequency technique described above, we obtain a comb of RF frequencies at the output of the interferometer with a spacing of approximately 2.8 MHz with a laser frequency scan rate of approximately 6 MHz/ms (fig. S2B) and a ramp duration of approximately 100 ms (this needs to be at least twice the round-trip time from the last repeater providing a loop-back signal). In order to extract the loop-back signal returned by an HLLB, the corresponding comb tooth must be spectrally filtered so that it can be processed. We achieve this, on a selection of frequencies, by downconverting the frequency to be measured with an RF mixer followed by a narrow band-pass filter, as in heterodyne receivers. As a local oscillator for the down-converting mixer, we use a programmable digital direct synthesizer board, which enables us to select the frequency to be down-converted (and hence the repeater along the cable). The down-converted signals are then measured by a synchronous multi-channel frequency counter.

Details about the UK-Canada submarine cable

Here we provide additional details on the submarine cable used for this work. The cable runs for approximately 1,000 km on the UK continental shelf and for 250 km on the Canadian shelf at a depth of less than 300 m. The remaining ~4,600 km of the cable runs in deeper water of depth up to 5,200 m. On the continental shelf, the cable was buried at a depth ranging from 0.3 to 1.8 m during its installation in early 2000s. However, over time the sediment layer can get removed by sea currents, exposing sections of the cable. Also, in hard seabed areas, the cable is not buried but

covered with rock dump, which might leave the cable partially exposed to water flow. For waters depth greater than 1,500 m the cable is simply laid on the seafloor. The optical cable is protected by a different level of armoring depending on water depth, ranging from heavy steel armor near the coastlines, where damage from ship anchors and fishing trawlers is more likely, to lightweight in deeper waters, where the cable diameter is only 17 to 22 mm. The cable crosses the Mid-Atlantic Ridge (MAR), where sea mounts emerge up to a water depth of approximately 2,300 m, at a cable length of approximately 2,100 km from the UK end.

Full set of span-wise measurements for the Northern Peru Mw 7.5 earthquake

Figure S4A shows the cable sections that were being measured during the Northern Peru earthquake on 28th November 2021. Figure S4B shows the signals detected in the time and frequency domain. The earthquake was not detected on the 3 sections on the cable located on the continental shelf, whilst it was detected on the other 6 deep water sections. The last panels of the time series and spectrograms (labelled "Entire cable") show the signal measured on the entire UK-Canada link. Here, the high level of environmental noise between 0.5 and 1 Hz prevents the detection of the earthquake.

Figure S5 shows a direct comparison between the optical signals detected on a single fiber span (S5 in Fig. 2C) and the signal recorded at seismic station PM.ROSA during the occurrence of the Northern Peru earthquake on 28th November 2021. This station is located in the Azores Island and is approximately 1,000 km away from the fiber. Amongst the body waves that are detected in the seismic station are the P, PP, S, SS, and the PKPPKP core phases. A long-period (< 10 s) Rayleigh wave is also observed arriving between the SS and the PKPPKP waves. For the span-wise measurements, only the direct P- and S-waves are confidently resolved. While the depth of the earthquake might explain why high-frequency surface waves are not observed in both signals, on the cable we observe lower sensitivity to signals with frequency < 0.1Hz for this earthquake. The same cable section did detect low frequency components for the Flores Sea earthquake. Further earthquake detections will allow to better understand and characterize the cable response to external perturbations.

More details on the back-projection method used for the Northern Peru Mw 7.5 earthquake

In the back-projection (BP) we used the IASP91 Earth model and mapped the product of envelopes of the time-reversed teleseismic P-waves to a horizontal source grid fixed at the hypocentral depth to search for the epicentral region that would cause the signals to add constructively (21). For this process, we assumed that the location of the detections is that of the mid-point of each fiber span to the earthquake catalog location. To calculate the envelopes, we band-pass filtered the signals between 0.5-2.0 Hz, estimated their time-frequency spectra, integrated them across the frequency axes, and normalized them to unit amplitude. This calculation provided us with a smooth measure of power as a function of time (Fig. S6). The spacing of the BP grid is 0.5-degrees and it extends all over the globe. The best-fitting source solution that is obtained through this exercise is ~2,000 km away from the earthquake catalog location. We attribute this difference to the poor azimuthal coverage of the fiber, the assumption of a 1D velocity model, and/or the distributed nature of the measurements.

Full set of span-wise measurements for the Flores Sea Mw 7.3 earthquake

Figure S7 shows the optical frequency deviations detected on 9 sections of the cable. The earthquake was not detected on cable sections near the MAR. We believe this might be due to the expected poor coupling of the cable with the seafloor due to the irregular bathymetry. Indeed, the intensity of the detected Northern Peru earthquake was lower for cable sections in this area. Similarly, to Fig. 3F, narrow-band features are observed on these cables sections which we attribute to cable movements due to currents or to pressure changes.

Comparison of frequency noise spectrum of spans used in 21st Oct 2021 measurements

In order to aid the comparison of the environmental noise levels detected by the spans of Fig. 3, in fig. S8 we plot the frequency noise power spectral density of a 10,000 s-long section of data for each span. For panels A, D and F we select data ranges to include tidal and current features.

Additional example of earthquake detection: Mw 7.3 Vanuatu earthquake

On 2nd Oct 2021 we detected a M7.3 earthquake with epicenter in Vanuatu on 4 cable sections (S2, S3, S4 and S5), as shown in Fig. S9. Figure S9 also shows the recorded ground motions at the seismic stations PM.ROSA (Azores Islands) and GB.CCA1 (UK). Epicentral distances along this part of cable range from approximately 149° to 151°, while PM.ROSA and GB.CCA1 are at similar distances of 153° and 151°, so provide a useful comparison with the signals recorded on the cable spans. The recordings on four of the five cable spans show a clear arrival that is consistent with the first arriving wave at PM.ROSA and GB.CCA1, which is expected to be the PKP phase that travels through the Earth's Core, followed by the depth phase pPKP. Since these phases arrive at steep incidence angles there is relatively little energy on the horizontal components of ground motion recorded at the two seismic stations. However, the arrivals on the cable sections show a significantly longer coda than on the vertical components at the seismic stations. The apparent signal duration on the cable may be increased by reverberation in the water column, as when a seismic wave arrives at the seabed, a large amount of its energy is transmitted to the water column, where it will reverberate (with little attenuation) for a long period of time (22,23). A longer coda following the initial PKP is observed on GB.CCA1.HHE perhaps because of conversions/reflections at the Moho and in the Crust.

Localization of dispersive noise sources

In Fig. 4A we showed the correlation between the wave height in the Irish Sea with the signals detected on the cable (cable sections of Fig. 4A and 4B, referred here as SC1 and SC2 respectively) in the 0.1-0.5 Hz frequency band. Below 0.1 Hz, dispersive primary microseisms are observed which can arise from distant ocean swells dispersing as the surface gravity waves travel across the ocean (24). For storm events where significant wave height (SWH) increases significantly, we can attempt to locate the source region by inspecting the dispersive signal for a possible distance from the receiver. We can also look at reanalysis data for areas of increased SWH in order to predict the

dispersion at that same receiver. In the example below, we have analyzed the dispersive primary microseism between 13th and 17th September 2021 on cable sections SC1 and SC2. By manually fitting a line to the dispersive signal and taking the endpoints as upper and lower frequency bounds of the dispersion, the group velocity v_g can be identified for waves in the deep ocean using the dispersion relation

$$v_g = \frac{g}{4\pi f}$$

where $g = 9.81\text{ms}^{-2}$ is the acceleration due to gravity and f is the frequency picked from the spectrogram. We pick the times t_1 and t_2 that the lowest and highest frequencies occur and solve the following simultaneous equations for the distance to the source d:

$$t_1 = t_0 + \frac{d}{v_{g1}}$$

$$t_2 = t_0 + \frac{d}{v_{g2}}$$

where t_0 is the origin time. Using the distance as a radius for the circle upon which the source might lie, we look for intersecting circles to deduce an approximate source location. Uncertainties in the line-fitting process results in an error of the calculated source distances ranging from 17% to 42% depending on the seismic station or cable section analyzed.

Figure S11 shows spectrograms of the signal detected on SC1 and SC2 as well as five land seismic stations in Ireland, Azores Islands, Canada and Greenland for comparison. After plotting the source radii from the two repeaters and three of the seismic stations in which the primary microseism shows, an overlap over Eastern Canada (Fig. S12) is identified. We are assuming the direction of travel for the energy packet followed the general circulation pattern of the North Atlantic. Intersections for these segment radii agreed with the land station radii. For dispersion prediction we looked at the ERA5 Reanalysis model for SWH from 9th to 16th September (25). At this time, Hurricane Larry was downgraded from a Category 2 to Category 1 system and the effect on sea state of this storm track is evident from the high SWH seen off the coast of Newfoundland on 11th September. This location correlates with the calculated source radii and the distance to each receiver station was measured from 46.5N,-52.5E. Predicted dispersion can be seen on Fig. S12 as green gradients and these agree with the dispersion signal gradients we have detected.

Supplementary Text

Architecture for simultaneous measurements on all the available cable spans

The modular nature of the frequency counter-based solution described above offered the flexibility required by initial testing of the technique. However, in order to achieve simultaneous measurements of all the available repeater-to-repeater spans of a cable, which can exceed 100 for intercontinental cables, future setups can be developed by using Field Programmable Gate Array

solution (FPGA), as shown in Fig. S3. By implementing the acquisition, filtering and frequency measurement of the loop-back signals within one or more FPGA chip, a low-cost and compact solution could be developed for deployment to a large number of cables.

Range extension

The combination of lossy return paths (HLLB) and the accumulation of Amplified Stimulated Emission (ASE) noise generated in each repeater along the cable can lead to a loop-back signal with marginal signal-to-noise ratio (SNR). In our current setup this can limit the range of repeaters from which a useable loop-back signal can be obtained. These limitations can be overcome with the following hardware improvements. In the current set-up (Fig. S2C), the EOM generates a carrier-suppressed double sideband signal (CS-DSB). By means of an acousto-optical modulator (AOM) we utilize only the upper of the two sidebands, to overcome the limitation due to EOM residual amplitude modulation (RAM), which creates spurious signals in the same frequency range of the loop-back signals. The AOM, which is inserted in the reference arm, shifts the optical beats so that the RAM components, which remain un-shifted, can be separated. By high-pass filtering at the AOM frequency we can select the upper sideband only. However, the lower sideband still contributes to the maximum optical power that can be injected in the fiber. This needs to be below thresholds set by the cable operator to avoid uneven distribution of the optical amplifier gain across the optical spectrum, cross talk and non-linear effects that could potentially affect the other channels carrying data traffic. By employing single sideband modulation in future setups, the power of the unused lower sideband will be transferred into the sideband used for generating the loop-back signals. The resulting additional injected optical power will lead to a higher SNR in the interferometric loop-back signal.
An alternative solution, where a laser source is phase locked to a scanning EOM sideband with high feedback bandwidth, could be employed. In this case, by generating a single scanning optical frequency, no power is wasted on residual carrier and unused sidebands. In this case all the injected power is utilized, resulting into a higher SNR of the returned signal.

A further significant range improvement can be achieved with the FPGA solution discussed above. In the current setup we use frequency counters to detect changes in loop-back signals. The counters work by detecting the zero crossings of the applied signal. This requires a sufficiently high SNR for the timing of crossing to be identified correctly. With an FPGA-based solution, advanced signal processing solutions can be implemented, to extract the phase/frequency changes of the loop-back signals, enabling measurements at SNR levels currently insufficient for the frequency counters.

Overcoming polarization-induced SNR degradation of the loop-back signals

In our current setup, the returned optical loop-back signals are combined with the local swept laser to produce a measurable RF beat. When the polarization of the returning signal is misaligned to that of the local source the SNR of the resulting RF beat degrades. Each optical signal received after being returned by the HLLB exhibits a different polarization state because it travelled through a different optical path. This leads to some loop-back RF beats with sufficient SNR and others with SNR below the required threshold for the frequency counter to perform a correct measurement. Polarization-diversity coherent receivers can be employed which, by combining the

local source and returned signals orthogonal polarizations, produce at least one useable signal at each point in time, for each loop-back signal. As this solution requires a double number of frequency counter channels, it was not implemented in the work presented here as additional counter channels were not available in our current set up. In an FPGA-based solution, as discussed above, frequency counters would no longer be required. By combining a polarization diversity receiver with an FPGA-based signal processing unit, as commonly done in modern telecommunication receivers, a very compact solution could be implemented.

Contribution of the laser frequency noise to the measurement noise floor

The HLLB loop-back signal in our experimental setup is obtained by interference between the returned optical signal and the local laser source. The return signal experiences a delay that is proportional to the optical path length of the Southport-HLLB-Southport loop. This can be illustrated as in the figure below

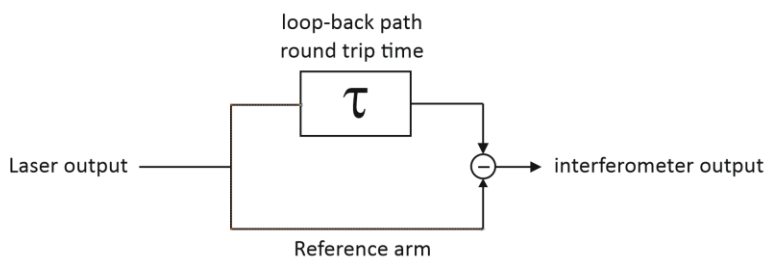

where τ is the delay experienced by the light that has travelled in the loop-back path and can be calculated as

$$\tau = \frac{2nL}{c}$$

where n is the effective group index, L is the length of fiber to the repeater and c is the speed of light. Because of the delay in one of the arms of the interferometer, frequency deviations of the laser source result in a phase change of the output of the interferometer. This arrangement is commonly known as “self-homodyne”, or “self-heterodyne” when one of the two arms of the interferometer is frequency-shifted, as in our experimental setup. For time scales significantly slower than τ, the self-heterodyne phase noise can be calculated as

$$\Delta\phi = \phi(t) - \phi(t-\tau) \approx \tau\frac{d\phi}{\mathrm{dt}} = 2\pi\tau\,\nu$$

Where $\Delta\phi$ is the phase noise measured at the output of the self-heterodyne interferometer and ν is the laser frequency noise. The frequency noise at the interferometer output can be calculated as

$$\eta = \frac{1}{2\pi}\frac{d\Delta\phi}{\mathrm{dt}} = \tau\,\frac{d\nu}{\mathrm{dt}}$$

It follows that the PSD of the self-heterodyne frequency noise and laser frequency noise are related as

$$S_\eta(f) = (2\pi\tau f)^2 S_\nu(f)$$

From the relationship above, the self-heterodyne noise that will be present on the loop-back signals of our experimental setup can be computed. In order to estimate the contribution of the laser instability to the measurement noise floor, we measured the frequency noise of a compact commercially available narrow-linewidth laser at 1542 nm against an Ultra-Low Expansion (ULE) cavity-based ultrastable laser at NPL. The computed self-heterodyne noise for a loop-back optical path length of 90 km, corresponding to the maximum span length typically found in more modern submarine cables, is shown in fig. S10. For comparison, we also show the measurement noise floor can be achieved with research-grade acetylene-locked lasers and ULE cavity-stabilized lasers.

Prospects for tsunami detection

The detection of off-shore earthquakes with submarine cables could provide additional life-saving warning time in a tsunami event by detecting the event closer to its epicenter (6). However, the ability to detect deep-water currents and pressure changes could potentially enable direct detection the tsunami as it propagates through the deep ocean rather than being inferred from seismic data.

Furthermore, by using span-wise measurements enabled by the technique shown in this work, the density of coastal sensors could be substantially increased. We have shown that the technique is sensitive to sea state, and in particular wave height, on a shallow continental shelf. These marine areas can extend hundreds of kilometers from coastlines. Tide gauge data and water level measurement are already monitored in areas prone to ocean hazards such as tsunami (*26*) but the density of dedicated sensors is low considering the area that would benefit from the coverage (*27*). By improving monitoring density through utilizing existing submarine cables the near-coastal tsunami signature could be improved and more reliable estimates of areas at imminent risk of tsunami could potentially be made. In this way, the spatial extent of coastal alerts could potentially be made more accurate, reducing the number of false alarms and thereby limiting complacency towards disaster alerts.

Monitoring deep-water temperature for global warming research

The thermal sensitivity of the optical path length of optical fibers could potentially be exploited to measure the long-term temperature variations of the seafloor for climate change and global warming research. Temperature and pressure changes convert into an optical path length of the fiber. We can estimate the expected changes on the index of refraction caused by expected temperature and pressure changes. For a typical telecommunication optical fiber, the sensitivity of the index of refraction to temperature changes is approximately 1 x 10^{-5}/K (*28*). Typical temperature changes measured on the sea floor have been measured to be in the range from 10 to 200 mK over timescales of several years (20). A temperature change of 10 mK corresponds to a change of the optical fiber index of refraction of 10^{-7}. The pressure sensitivity of telecommunication optical fiber is of the order of 10^{-11}/Pa (*29*). For water depth larger than 1500 m, the absolute change on the seafloor is typically less than 1 kPa over several years (30). This would lead to a change in the optical index of refraction at the 10^{-8} which is still one order of magnitude smaller than the change due to temperature. By monitoring the phase changes over long time scales, the average temperature variation of the span under test could be obtained. The

sensitivity of our current setup is sufficient to measure phase changes equivalent to temperature changes at the mK level of a 90 km span over 1 day of averaging. A possible limitation over very long-time scales might arise from relaxation of internal stresses of the cable, but no data is available at present to estimate the magnitude of this effect and more research is needed.
A temperature monitoring array based on submarine cables would allow to map the seafloor temperature with a spatial resolution, along the cable, equal to the span length (45 to 90 km). We stress that only the variation of temperature can be obtained rather than the absolute value. For absolute temperature measurements, a calibration could be performed in situ during measurement campaigns with deep ocean standards thermometers. However, for climate change and global warming research the measurement of seafloor temperature changes over time is of great importance. As the time scales involved in climate change observations are orders of magnitude larger than the time constants involved in heat propagation in the cable, we believe the cable structure does not affect the temperature reading.

Additional acknowledgments

We acknowledge the Danish National Metrology Institute (DFM) for providing the raw data for the StabiLaser frequency noise. The ERA5 data set was downloaded from the Copernicus Climate Change Service (C3S) Climate Data Store. The facilities of IRIS Data Services, and specifically the IRIS Data Management Center, were used for access to waveforms, related metadata, and/or derived products used in this study. IRIS Data Services are funded through the Seismological Facilities for the Advancement of Geoscience (SAGE) Award of the National Science Foundation under Cooperative Support Agreement EAR-1851048. The results contain modified Copernicus Climate Change Service information 2020. Neither the European Commission nor ECMWF is responsible for any use that may be made of the Copernicus information or data it contains. Cable data for submarine cable map: TeleGeography’s Telecom Resources licensed under Creative Commons Share alike.

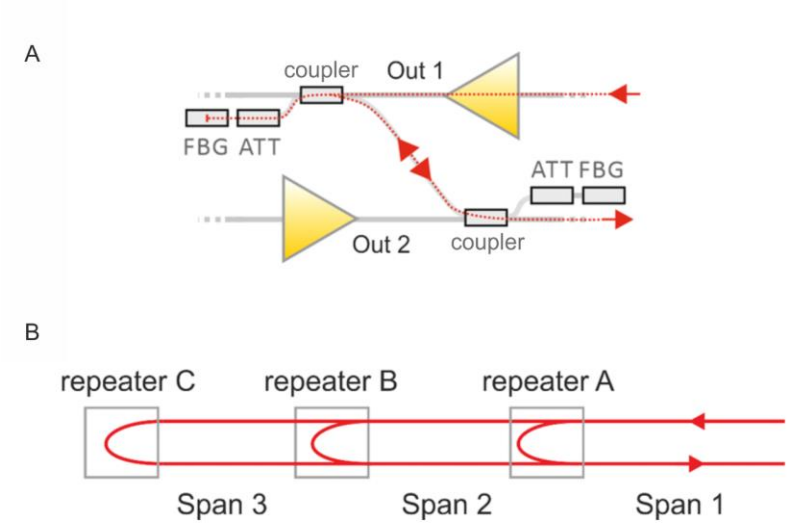

Fig. S1. Submarine cable loop-back topology. (A) Top-level illustration of the loop-back architecture used to extract localised environmentally-induced signals in the submarine cables. (B) Details of the HLLB topology. ATT: attenuator; FBG: Fibre Bragg Grating.

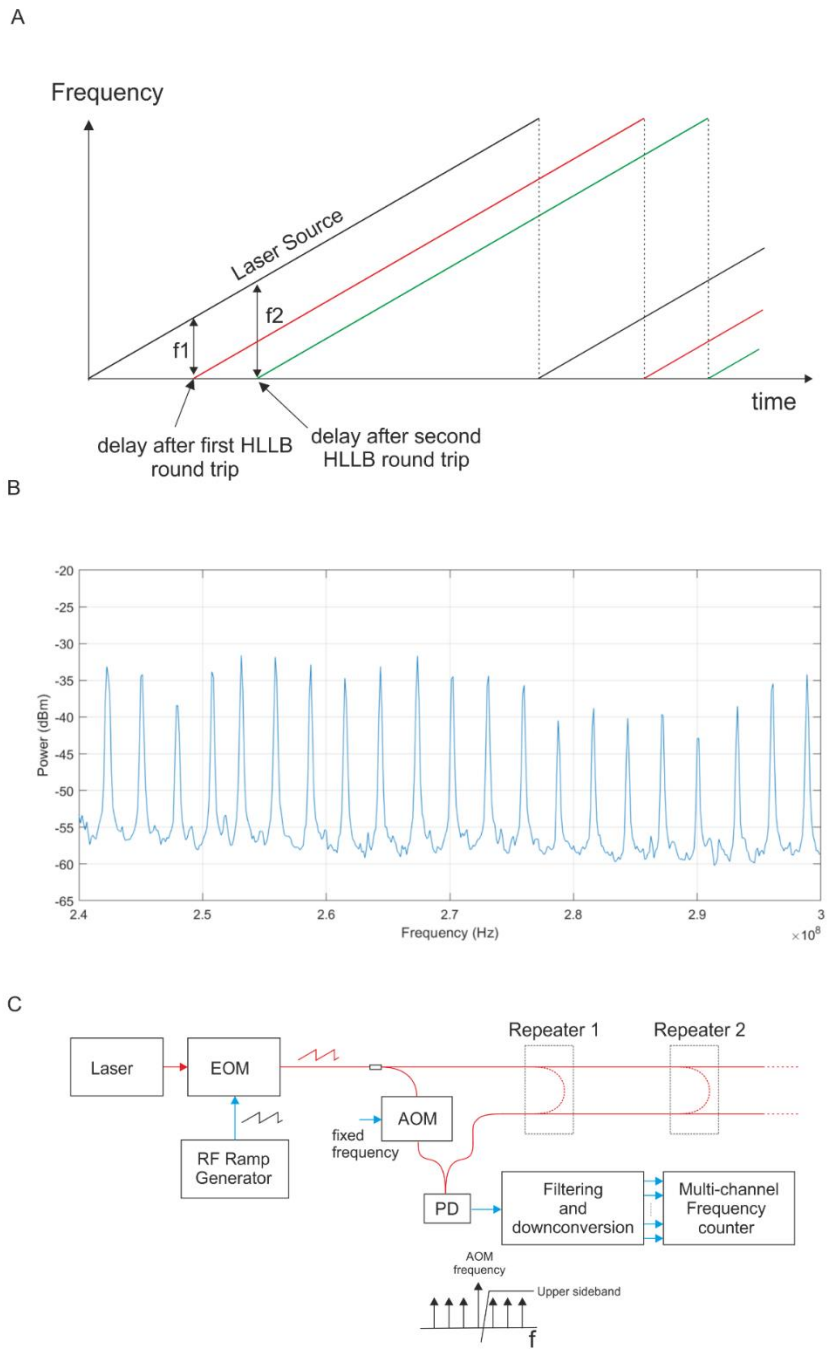

Fig. S2. Operating principle of the frequency-swept technique for the extraction of the loop-back signal from each repeater. (A) Illustration of the operating principle that enables return signals from HLLBs to be separated in the frequency domain. Because of the different delay experienced by each loop-back optical signal, the resulting frequency difference from the comparison with the local swept frequency laser source is different for each repeater. (B) A portion of the comb frequency spectrum generated at the output of the interferometer, measured with a 100 kHz resolution bandwidth (C) Diagram of the experimental setup. EOM: Electro-optic modulator; AOM: Acousto-optic modulator; PD: Photodiode; RF: Radio-frequency.

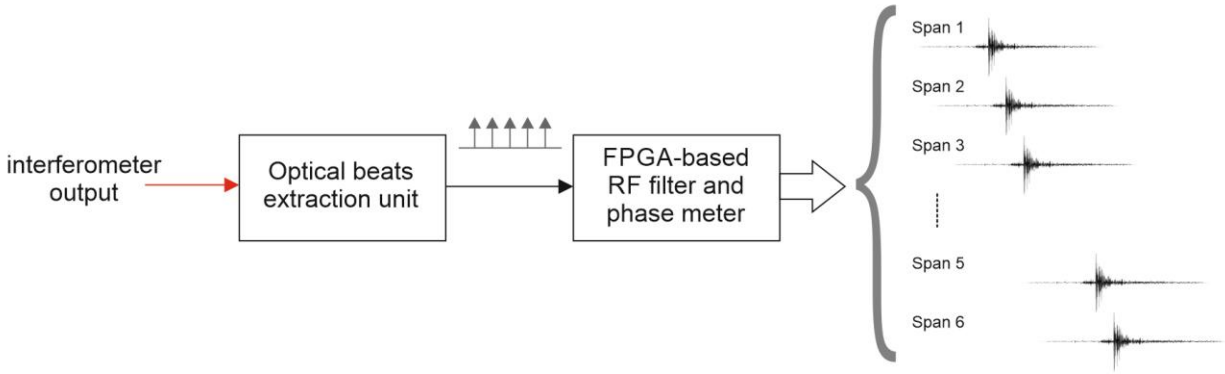

Fig S3. Diagram of the FPGA-based solution that enables the simultaneous monitoring of all the spans of the cable. An FPGA-based solution for implementing the filtering and phase extraction of the loop-back signals enables the technique used in this work to be scaled up in a compact and cost-effective way for its implementation to a large number of cables.

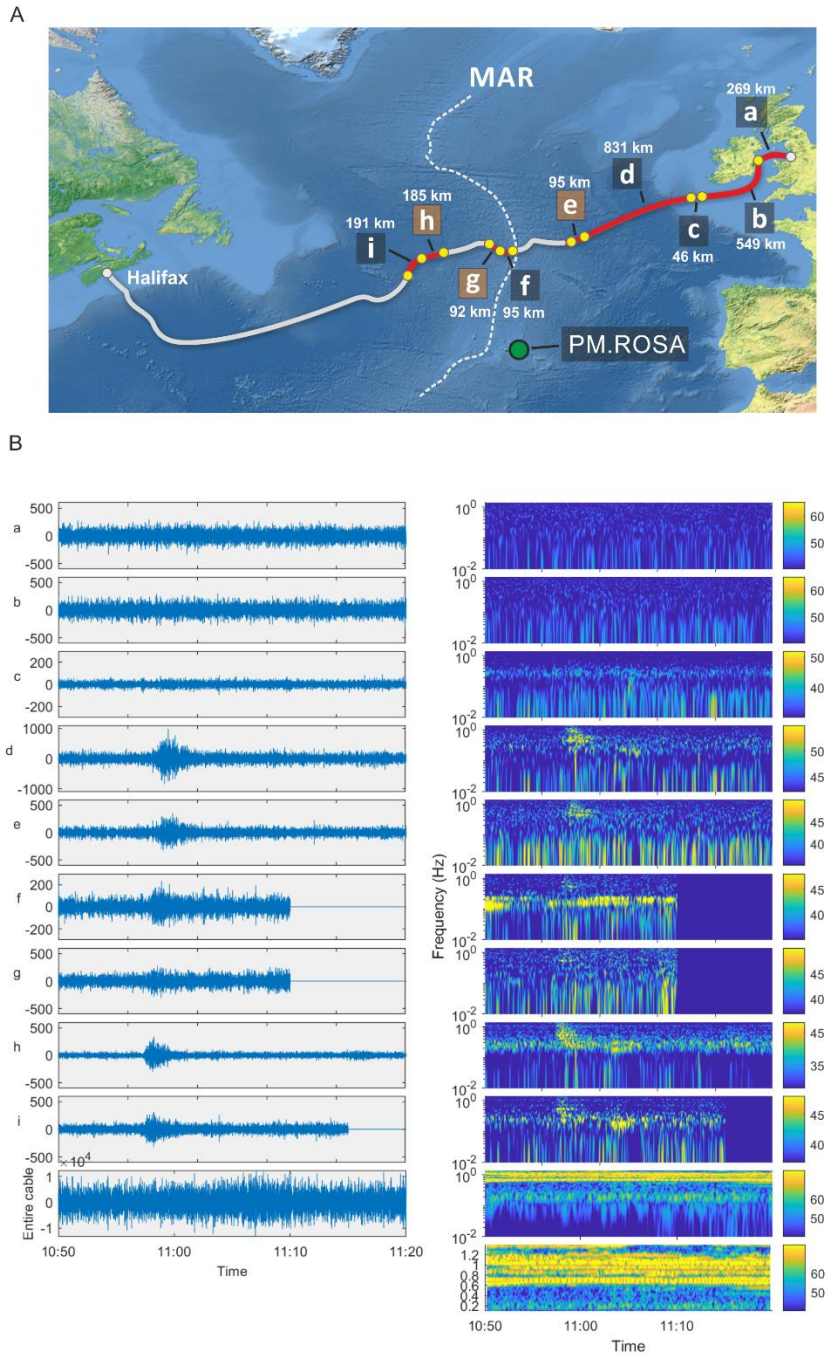

Fig. S4. Detection of the Northern Peru earthquake. (A) Map of the cable sections used in this measurement. Sections e, g and h correspond to sections S3, S4 and S5 in Fig. 2C. (B) Time series and spectrograms of the signals detected on the 9 spans under test. The panels labelled "Entire cable" shows the time series and spectrogram of the signal detected on the entire UK-Canada. The right bottommost panel shows the spectrogram of the same signal but on a linear scale for better visualization of the higher frequency range (0.2-1.4 Hz). The signal on the entire UK-Canada cable shows a high level of noise preventing the earthquake to be resolved.

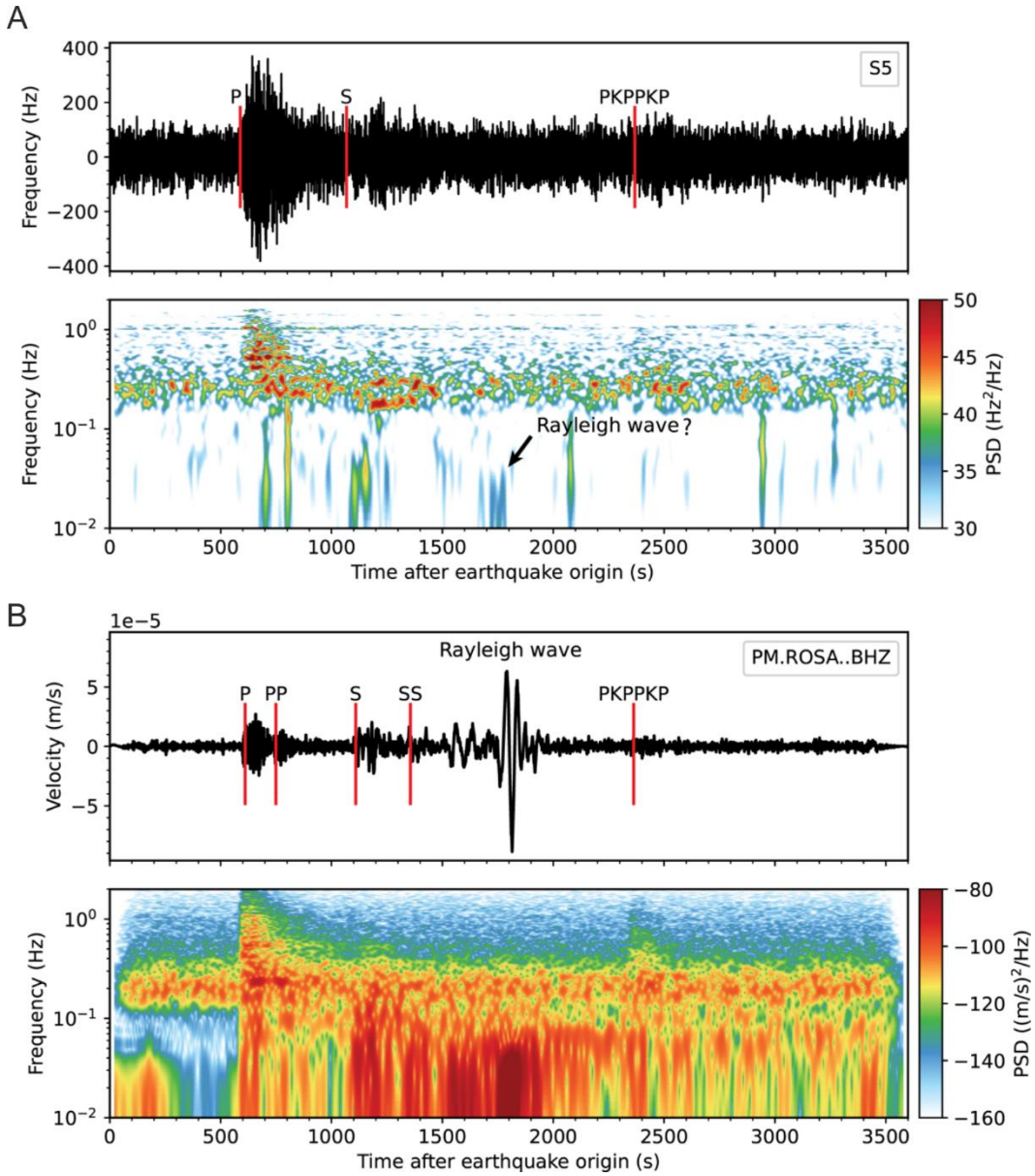

Fig. S5. Comparison between span-wise and seismic measurements for the Northern Peru earthquake. (A) Optical deviations recorded during the Northern Peru earthquake at fiber span S5. (B) Velocity recording of the Northern Peru earthquake at station PM.ROSA in the Azores Island. The vertical red lines in each panel mark the theoretical earthquake wave arrivals. The high-frequency (> 0.1 Hz) P and S direct arrivals are visible on the cable section. Low frequency components corresponding to the P, PP, S, S and Rayleigh wave arrivals are also detected on the cable sections but with low intensity.

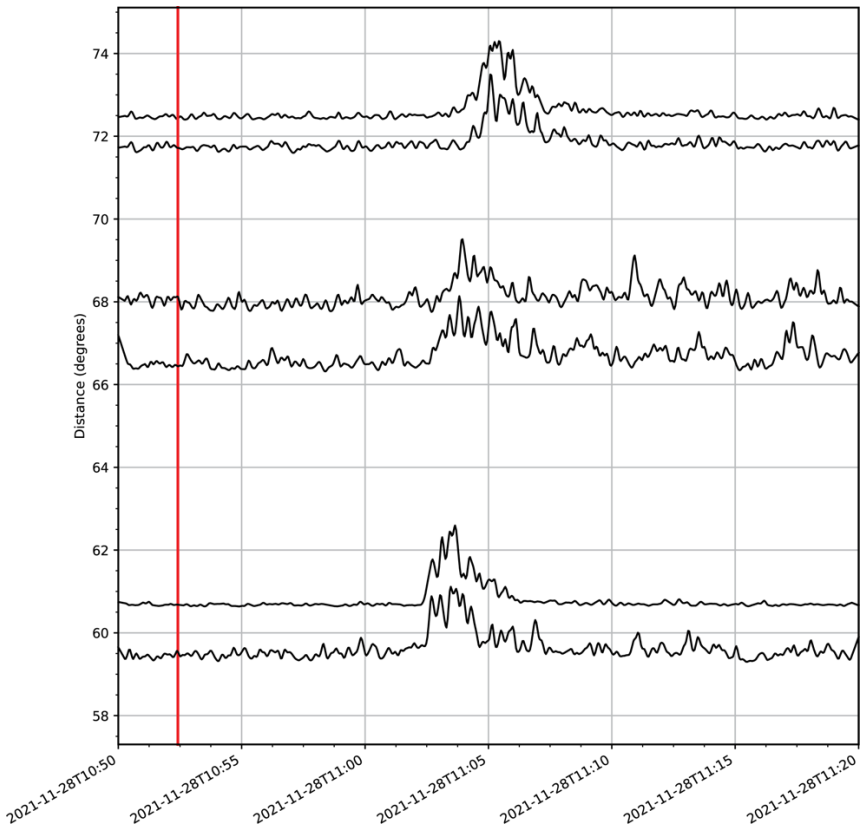

Fig. S6. Envelope signals of the Northern Peru earthquake used in the back-projection. The traces are organized by their distance from the earthquake to the closest point of each fiber span. The red line marks the origin time of the earthquake.

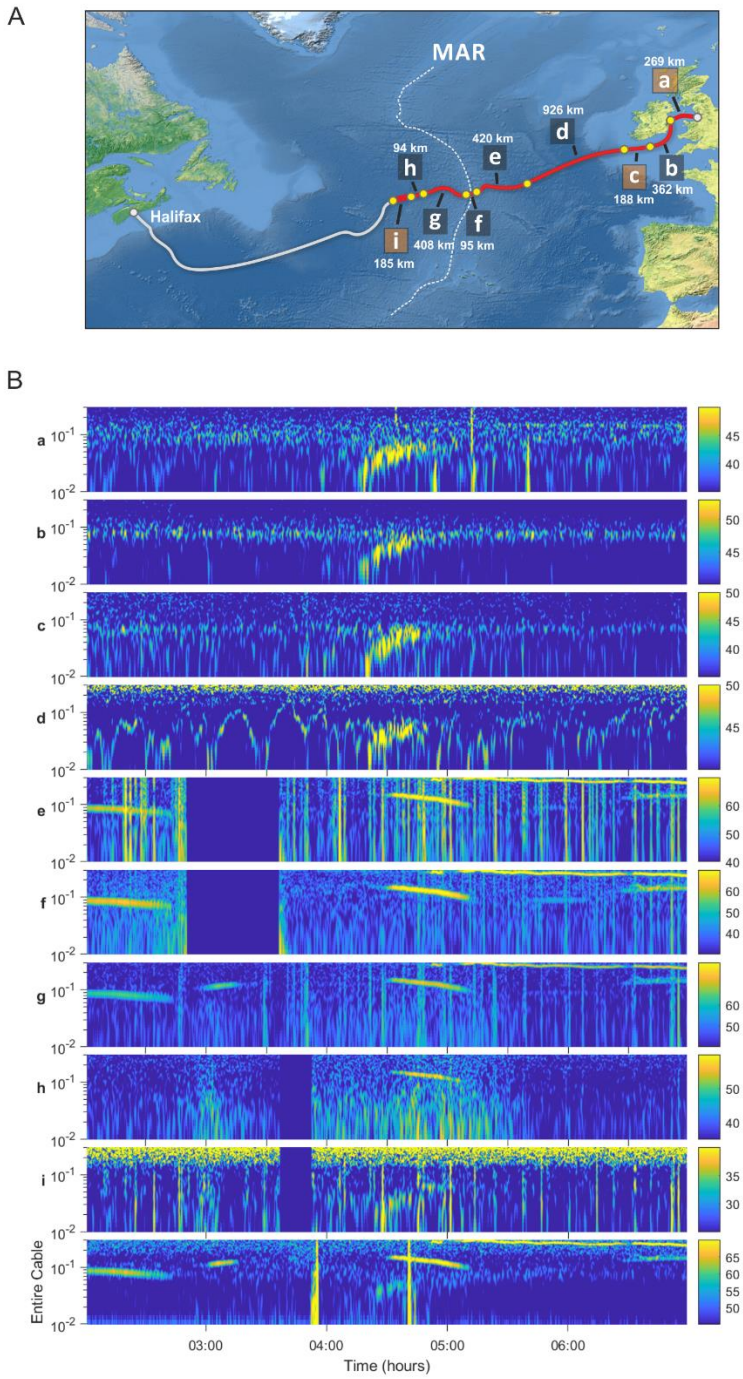

Fig. S7. Signals measured on 9 sections of the submarine cables during the Flores Sea earthquake. (A) Map illustrating the cable sections used for this measurement. Section a, c and i correspond to the sections marked S1, S2 and S5 of Fig. 2C. (B) Signals measured on the cable sections. The earthquake was detected on spans a to d and i. The last panel (labelled "Entire cable") shows the earthquake detected on entire Southport-Halifax link.

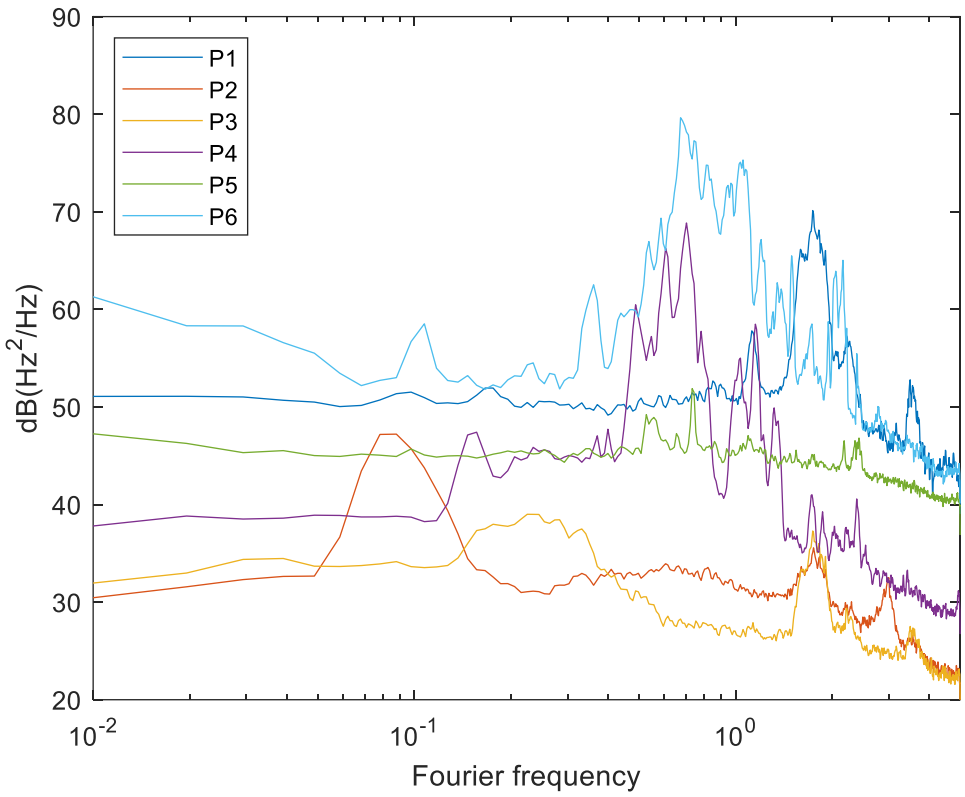

Fig. S8. Frequency noise spectrum comparison of the signals detected on the spans of Fig 3. The label P indicates the panel number of Fig 3 from top to bottom.

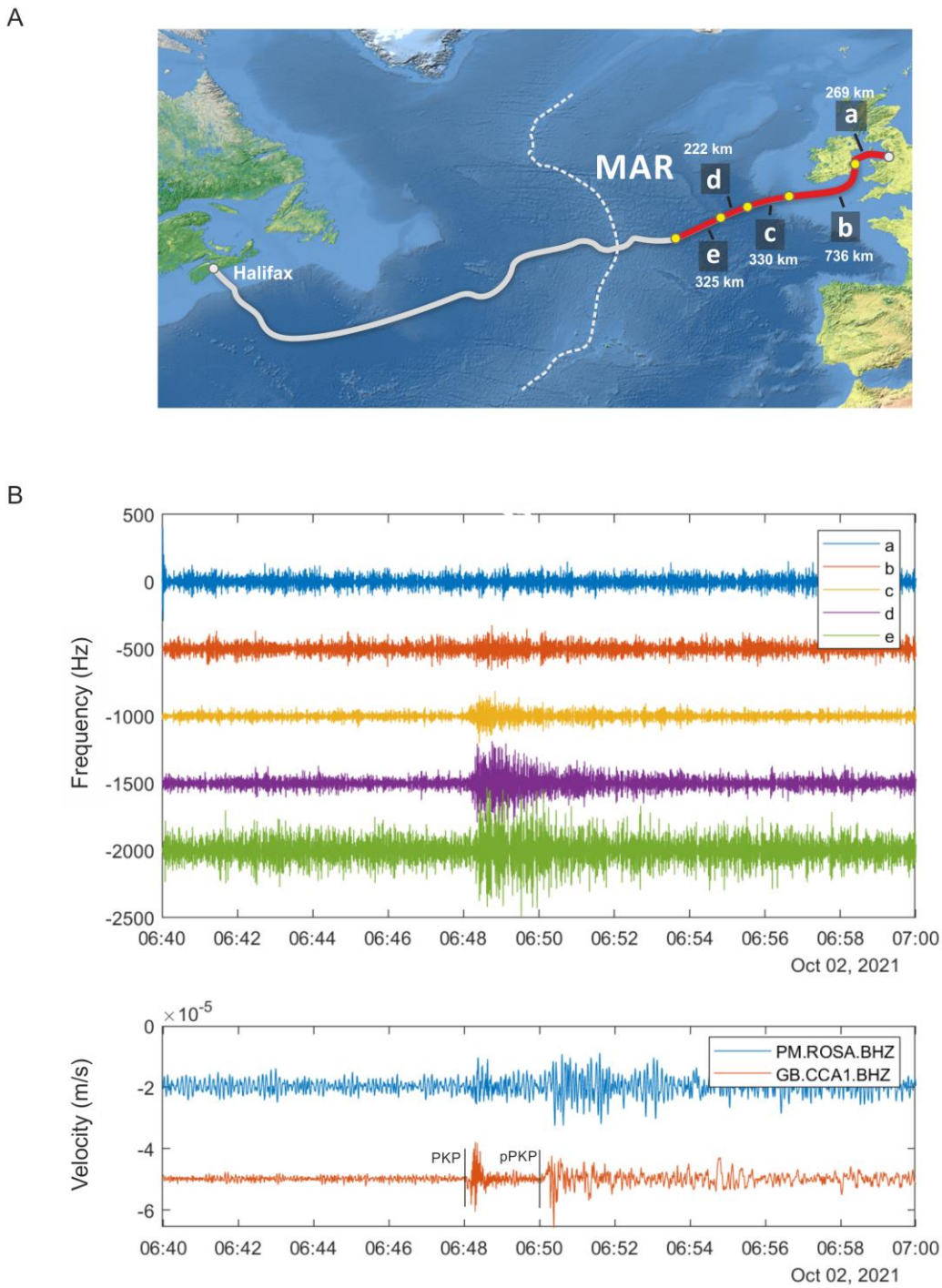

Fig. S9. Detection of the M7.3 Vanuatu earthquake on 2 Oct 2021 on 4 different sections of the UK-Canada cable. (A) Maps of the cable sections under test. (B) Comparison between the signals detected on the cable and seismic stations on land in UK and Azores Islands. Traces are offset from each other to aid visualization.

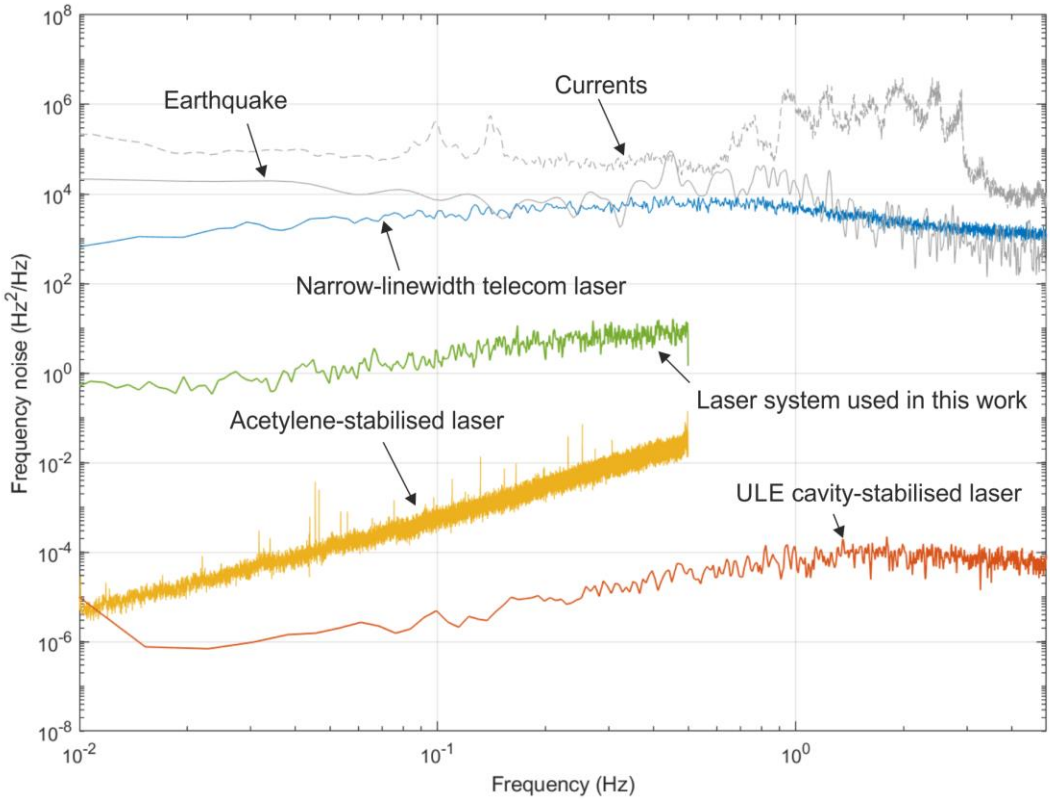

Fig. 10. Comparison of laser noise contribution to the measurement noise floor for different laser stabilization technologies. Calculated self-heterodyne noise for a good quality narrow-linewidth telecommunication laser, an acetylene-stabilized laser (StabiLaser, Danish Metrology Institute), the research-grade laser used in this work and a typical NPL ULE cubic cavity-stabilized laser. The self-heterodyne noise was calculated for a span length of 90 km from measured frequency noise data for each laser.

.

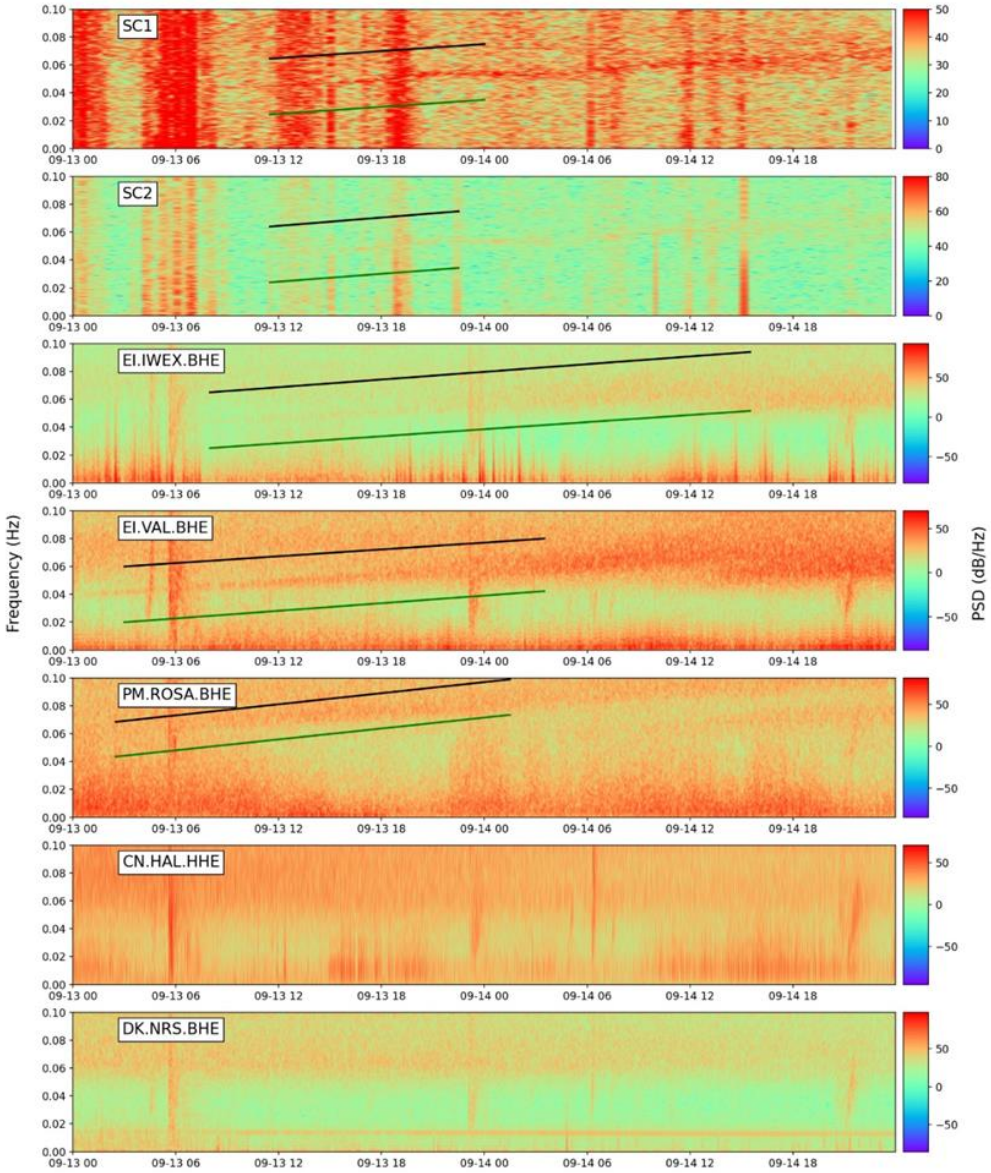

Fig. S11: Spectrograms for the two cable segments and five seismic stations (East component). CN.HAL and DK.NRS show no comparable dispersive signal. Black lines are gradients picked in order to find the source distance. Green lines are gradients calculated from ERA5 SWH shown in figure S11. Both gradient lines are offset so as not to obscure the microseism.

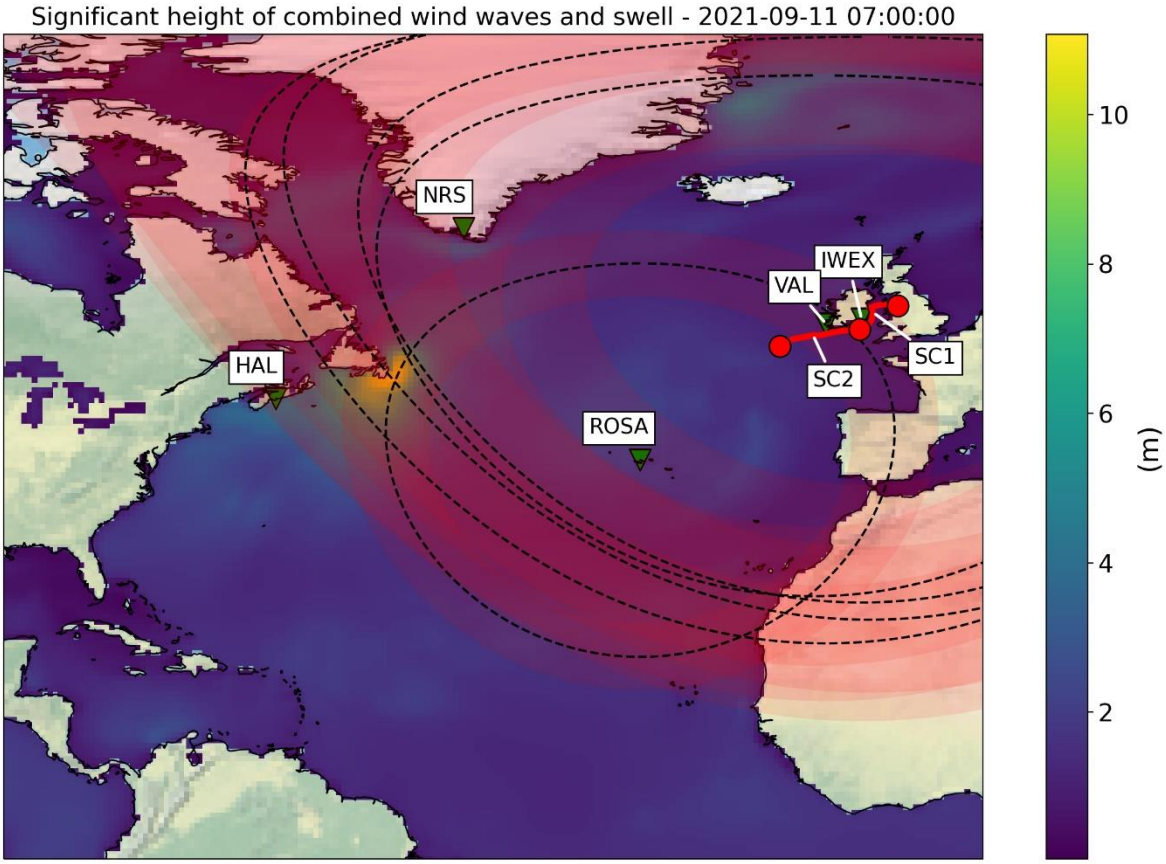

Fig. S12: Possible source locations and significant wave height in the North Atlantic. Black dashed lines indicate the calculated potential source radii with shaded red areas representing the error for each. Green triangles are seismic stations and cable segments SC1 and SC2 are represented by red lines. There are no radii for HAL or NRS due to the absence of the primary microseism at these locations. High SWH at the intersection is plotted with the distance to receivers measured from 46.5N, -52.5E.

Fig S13. Map of the existing and planned submarine cables.